Analyzing Nitrogen in Silicate Glasses by Secondary Ion Mass Spectrometry

by

Margo Elaine Regier

A Thesis Presented in Partial Fulfillment
of the Requirements for the Degree
Masters of Science

Approved April 2016 by the
Graduate Supervisory Committee:

Richard Hervig, Chair
Kurt Roggensack
Christy Till

ARIZONA STATE UNIVERSITY

May 2016

ABSTRACT

Volcanic devolatilization is one of the major processes in the global nitrogen cycle. Past studies have often estimated the magnitude of this flux using volcanic emission measurements, which are limited to currently active systems and sensitive to atmospheric contamination. A different methodological approach requires appropriate analytical parameters for nitrogen analysis in silicate glasses by secondary ion mass spectrometry (SIMS), which have not yet been established. To this end, we analyze various ion implanted basaltic and rhyolitic glasses by SIMS. We demonstrate that water content significantly affects the ion yields of $^{14}N^+$ and $^{14}N^{16}O^-$, as well as the background intensity of $^{14}N^+$ and $^{12}C^+$. Application of implant-derived calibrations to natural samples provide the first reported concentrations of nitrogen in melt inclusions. These measurements are from samples from the Bishop Tuff in California, the Huckleberry Ridge Tuff of the Yellowstone Volcanic Center, and material from the Okaia and Oruanui eruptions in the Taupo Volcanic Center. In all studied material, we find maximum nitrogen contents of less than 45 ppm and that nitrogen concentration varies positively with CO_2 concentration, which is interpreted to reflect partial degassing trend. Using the maximum measured nitrogen contents for each eruption, we find that the Bishop released $>3.6 \times 10^{13}$ g of nitrogen, the Huckleberry Ridge released $>1.3 \times 10^{14}$ g, the Okaia released $>1.1 \times 10^{11}$ g of nitrogen, the Oruanui released $>4.7 \times 10^{13}$ g of nitrogen. Simple calculations suggest that with concentrations such as these, rhyolitic eruptions may ephemerally increase the nitrogen flux to the atmosphere, but are insignificant compared to the 4×10^{21} g of nitrogen stored in the atmosphere.

ACKNOWLEDGMENTS

I thank Dr. Richard Hervig for being the master of SIMS, Dr. John Stix and Dr. Gregor Lucic at McGill University for providing FTIR spectra for the rhyolitic glasses, Dr. Kurt Roggensack for providing FTIR spectra and electron microprobe data for the basaltic suite of glasses, and Dr. Kenny Befus, Madison Myers, Dr. Colin Wilson, Dr. Paul Wallace, and Dr. Michael Rowe who provided comments, samples, electron probe measurements, and/or FTIR-determined H_2O and CO_2 measurements of Bishop melt inclusions. Research was supported by the Mineralogical Society of America's Student Grant in Mineralogy and Petrology and NSF grant EAR1362996 to the ASU SIMS Facility.

TABLE OF CONTENTS

LIST OF TABLES

LIST OF FIGURES

Chapter 1

INTRODUCTION

1.1 Nitrogen Cycling and Solubility

The foundation of a geologic nitrogen cycle requires well-constrained reservoir estimates and a thorough understanding of the fluxes between these reservoirs. Estimates of nitrogen contained within the crust and mantle have large uncertainties, but together, are larger than that of the atmospheric reservoir (Fig. 1; Johnson and Goldblatt, 2015). Similarly unconstrained is the origin of nitrogen in the mantle. Two distinct models have recently been proposed. The first model invokes large scale nitrogen storage as a consequence of magma ocean crystallization and a subsequent flux from mantle to atmosphere with the onset of subduction and mantle wedge oxidation (Li et al., 2013; Mikhail and Sverjensky, 2014). The second model posits that mantle nitrogen is the consequence of a large input following the onset of subduction (Goldblatt et al., 2009). This model estimates higher N_2 partial pressure in the early atmosphere, which would provide a partial solution to the faint young sun paradox (Goldblatt et al., 2009; Wordsworth and Pierrehumbert, 2013). However, recent analyses of 3 to 3.5 Ga fluid inclusions have been used to propose that the N_2 content of the atmosphere has remained constant for the majority of earth's history (Marty et al., 2013).

In contrast to the elusive origin of mantle nitrogen, a large amount of crustal nitrogen was likely sourced from a draw down of the atmospheric reservoir. This crustal sequestration could only have started following substantial continental growth,

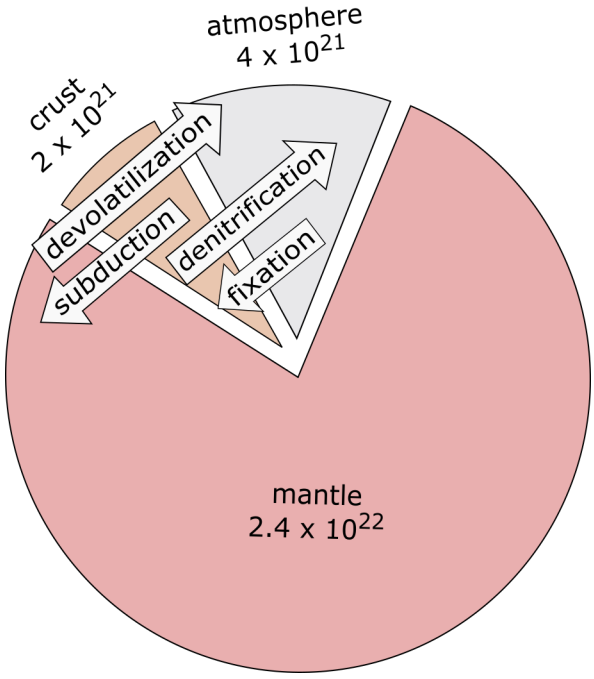

Figure 1. Approximate masses, in grams, of nitrogen for the three major global reservoirs and processes that link them. Estimates of concentrations for the upper and lower continental crust are 150 ± 18 ppm and 17 ± 1 ppm, respectively and 6 ppm for the mantle (abundances from Johnson and Goldblatt, 2015; figure after Canfield et al., 2010).

but may have predated the evolution of nitrogen-fixing organisms, via the alternative of lightning fixation (Raymond et al., 2004). The evolution of biological fixation likely accelerated this process, culminating in the highly efficient biological fixation systems of today, which have the potential to sequester all atmospheric nitrogen into the crust in 100 Ma, absent crustal outputs (Cartigny and Marty, 2013).

Devolatilization is one of the important processes that offsets the subduction-related input of nitrogen into the mantle and the fixation and sequestration of nitrogen into the crust. However, the stability of this flux over geologic time and how variables can affect its efficiency are relatively unknown. Prior attempts to quantify the volcanic devolatilization flux have often used N_2/noble gas systematics from volcanic and geothermal gases, water, and vapor condensate samples (Sano et al., 2001; Hilton

et al., 2002; Elkins et al., 2006), which are limited to currently active systems, sensitive to surface contamination, and may not be appropriate due to the various nitrogen species present in mantle and crustal conditions (Mikhail and Sverjensky, 2014). Crushing and combustion of glass for nitrogen analysis has proven useful for mid-ocean ridge basalts and back arc basalts (Marty, 1995; Sano et al., 2001), but these glasses may have already released a substantial amount of their nitrogen prior to quenching. Trapped parcels of melt in phenocrysts, called melt inclusions (MI), offer an alternative, potentially more pristine, source for measuring pre-eruptive magmatic concentrations of nitrogen. While care must be taken to select those inclusions that have little post-entrapment modification (Wallace, 2005, and references therein), analysis of these parcels is commonly used to place constraints on volatile fluxes (Wallace, 2005), elucidate depth of entrapment (e.g. Roggensack et al., 1997), and identify inputs of new magmatic material (e.g. Dunbar and Hervig, 1992).

The use of melt inclusion analysis for global flux calculations is complicated by the tendency of low solubility volatiles, such as CO_2, to efficiently exsolve before melt inclusion entrapment (Wallace, 2005). Nitrogen physically dissolves within silicate networks under crustal pressures and oxidizing conditions as N_2 (Mulfinger, 1966; Mulfinger et al., 1972; Libourel et al., 2003; Miyazaki et al., 2004). The solubility of this molecule can be estimated using ionic porosity models, which produce results nearly identical to that of argon because of its similar covalent radius. One such ionic porosity model for hydrous rhyolites (Nuccio and Paonita, 2001) suggests that even when CO_2 is 80% degassed, $\sim$80% of the initial N_2 will remain in the melt. Nevertheless, the presence of a vapor phase containing some amount of nitrogen during inclusion entrapment is likely, so all measured nitrogen contents in inclusions must be considered minimum estimates for initial magmatic concentrations.

Experimental studies have also provided solubility estimates (Table 1). While they are wide ranging, the values (60 to 200 ppm) are high enough to suggest that natural samples might contain concentrations measurable by secondary ion mass spectrometry (SIMS). Furthermore, preliminary results indicate that nitrogen diffusivity in quartz is equal to or less than that of carbon at temperatures below 1100°C (E. B. Watson, personal communication). Therefore, we can assume that negligible N_2 has diffused out of our host quartz crystal.

The inclusion of nitrogen in melt inclusion analyses can provide insights about cycling between the three major global reservoirs and can be used to elucidate multispecies degassing processes in magma chambers. However, to our knowledge, no analyses of nitrogen in melt inclusions have been published. To this end, we provide best practice suggestions for the analysis of nitrogen in various silicate glasses, and present measurements in three silicic systems, where the high nitrogen solubility presents measurable concentrations.

Table 1. Experimental estimates of nitrogen solubility in albitic melts at conditions relating to this study

	Kesson and Holloway, 1974	Tsipenyuk et al., 1997	Li et al., 2015*
T (°C)	∼956	1250	800
P (kbar)	2.1	3	2
fO_2 buffer	>NNO	NNO	>NNO
H_2O (wt.%)	Not reported	Not reported	10.2
N (ppm)	∼150	∼60	65-193

*May have not reached equilibrium as suggested by the authors

1.2 Samples Selected for Study

In order to develop calibrations for variably hydrated natural glasses, basaltic and rhyolitic glasses with a range of water contents were studied. Glasses include five experimentally-hydrated rhyolites (M3N, M6N, 2, 4, and 6) synthesized in an internally heated pressure vessel (H.R. Westrich, personal communication) from Panum Crater Dome (PCD) natural obsidian starting material. Also included in our samples are volatile-saturated basalts (z19, x61, x103, x107) that were produced from one starting composition under 3.1-6.1 kbars and 1150-1190°C in piston-cylinder single capsules of $Au_{80}Pd_{20}$ (after Moore et al., 2008). Major element starting compositions for the basalts and rhyolites are given in Table 2.

An initial informal survey of melt inclusions revealed higher ion counts of nitrogen in rhyolitic compared to basaltic inclusions. Therefore, we focused this initial study on rhyolitic inclusions. More specifically, we report nitrogen concentrations from Bishop, Huckleberry Ridge, and Taupo Volcanic Center material, rhyolitic systems in distinct geological settings. The Bishop Tuff, erupted 760 ka, created the Long Valley Caldera in CA, and is composed of chemically-zoned Plinian tephra and ignimbrite (Hildreth and Wilson, 2007). The early erupted samples have high concentrations of H_2O (∼5.3 wt.%) and low concentrations of CO_2 (∼62 ppm), whereas the later erupted material contains lower concentrations of H_2O (∼4.1 wt.%) and variable CO_2 (∼150-1085 ppm) (Wallace et al., 1999). We include samples from the airfall deposits (F1-1a, F1-6a), middle airfall deposits (BB-105) and later ignimbrite deposits (327-3-1) of the Bishop Tuff (Dunbar and Hervig, 1992; Wallace et al., 1999; Christiansen, 2001). The ∼2200 km^3 Huckleberry Ridge Tuff (HRT) erupted 2.077 Ma in the Yellowstone Plateau Volcanic field (Singer et al., 2014). The samples in this study are those

immediately below member A and therefore represent some of the first erupted HRT (Christiansen, 2001). The third locality surveyed was the Taupo Volcanic Center on the North Island of New Zealand. This volcano lies within the southern extension of the Tonga-Kermadec subduction system and has experienced various large silicic eruptions and caldera collapse over the last 2 Ma (Wilson et al., 1984; Wilson et al., 1995). We focus on the moderately sized ∼1.5 km^3 Okaia tephra which was deposited around 28.6 ka, and the Oruanui supereruption (∼530 km^3), which occurred only ∼3 ka later (Wilson and Charlier, 2009; Lowe et al., 2013; Vandergoes et al., 2013).

Table 2. Starting composition of experimental rhyolitic and basaltic glasses

Major element	Natural rhyolite (wt.%)[1]	Starting basalt (wt.%)[2]
SiO_2	76.40(16)	49.36(21)
TiO_2	0.07(6)	1.17(3)
Al_2O_3	12.44(12)	17.33(13)
FeO	1.02(5)	9.32(17)
MnO	0.03(2)	0.17(4)
MgO	0.02(2)	9.46(13)
CaO	0.53(5)	9.01(9)
Na_2O	4.21(2)	2.97(9)
K_2O	4.68(15)	0.80(3)
P_2O_3	n.a.	0.38(3)
Sum	99.40(27)	99.97(36)

[1] Devine et al., 1995 [2]Basaltic composition was analyzed using a CAMECA SX50 electron probe microanalyzer at the University of Arizona with a 15 μm beam, 15 kV accelerating voltage, and 8-10 nA current for K, Na oxides, and 20 nA for other elemental oxides. 1 sigma errors are given in parentheses and are applicable to the last one or two decimals.

Chapter 2

N AND C IMPLANTS AND CALIBRATION DEVELOPMENT

2.1 Methodology

2.1.1 Species Selection and Background Control

Most SIMS measurements of hydrogen and carbon take advantage of the high negative secondary ion yields of $^{12}C^-$ and H^- or $^{16}OH^-$ (e.g. Hauri et al., 2002; Tenner et al., 2009). While nitrogen does not make a stable elemental negative ion, there are several molecular nitrogen ions available for secondary ion selection, including $^{28}Si^{14}N^-$, $^{14}N^{16}O^-$, and $^{12}C^{14}N^-$. There is not enough carbon in our glasses to generate a stable CN^- signal and the SiN^- species requires very high mass resolving power (MRP) for unambiguous separation from other molecular ions (resolving SiN^- from $^{41}KH^-$ requires >6,000 MRP and separating $^{26}Mg^{16}O$ from SiN^- requires >16,000 MRP). The NO^- species also requires a high resolving power of 5500 (Fig. 2), which significantly reduces the nitrogen counts. Measuring atomic $^{14}N^+$ using an O^- primary beam is limiting because the ionization potential for nitrogen is high. However, because separating N^+ from all potential interferences requires only 1200 MRP (Fig. 2), the identification of nitrogen is unambiguous without much signal loss.

In order to address the potentially high levels of background nitrogen and carbon, all samples reported here, except for one YSiAlON glass, were mounted in low volatile, high purity indium, and measured at high vacuum conditions (at or below 2 x 10^{-9} torr). However, substantial N^+ and C^+ backgrounds remained. In order to quantify

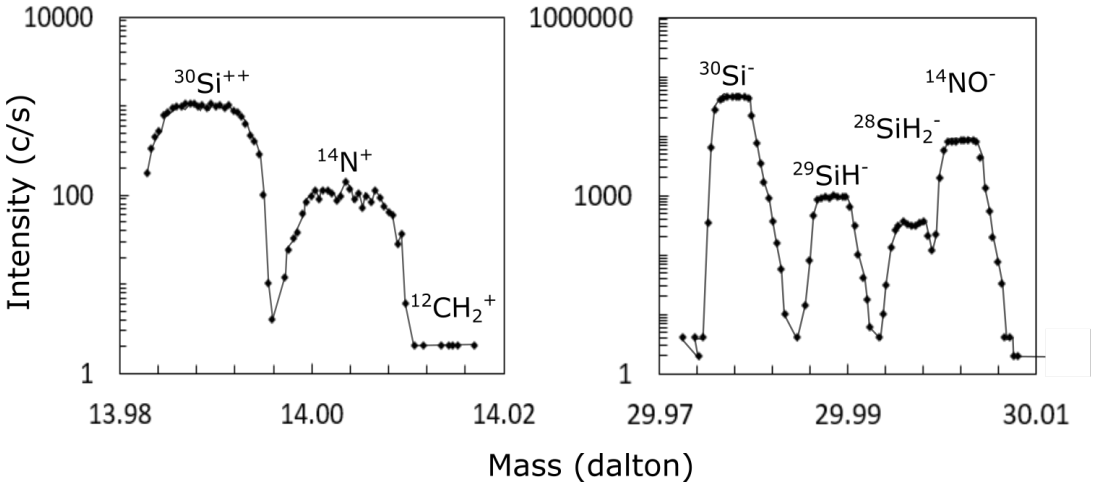

Figure 2. Mass spectra for $^{14}N^{+}$ and $^{14}N^{16}O^{-}$ on YSiAlON (containing 1.23 wt.% N) at 1200 and 5500 MRP respectively. Mass spectra on our basaltic and rhyolitic glasses appear similar, but with less intense nitrogen signals.

this background signal in different matrices, $N^{+}/^{30}Si^{+}$ and $C^{+}/^{30}Si^{+}$ intensities were monitored at various sputter rates during depth profile analysis of the low H_2O natural obsidian, PCD. Sputter rate was controlled by changing the raster sizes from 120 x 120 μm to 45 x 45 μm. The analyzed area was scaled to $\leq 2/5$ the raster size using field apertures. Sputter rate was later quantified using a stylus or optical profilometer at Arizona State University to measure crater depths. Accuracy of the sputter rate is limited by the accuracy of the profilometers which was tested on step height standards to be better than $\pm$ 3%.

2.1.2 Implants and Calibration Calculations

Due to a paucity of nitrogen standards in silicate glasses, and the difficulty of detecting low concentrations of nitrogen using other analytical methods, we chose to create standards using ion implantation by Leonard Kroko, Inc. (Tustin, CA).

Implantation, common in semiconductor doping, involves introducing a dose (or fluence, in atoms/cm^2) of a particular ion at depth within a chosen matrix (Grob, 2013). Both carbon and nitrogen were implanted to test the effect of water on their calibrations and to produce indium-mounted standards. Because the yields of N^+, NO^-, and C^+ are low, we chose relatively high fluences of 2.5 x 10^{15} and 5 x 10^{15} atoms/cm^2 for carbon and nitrogen respectively, providing peak concentrations of $\sim$0.3 wt.% nitrogen and $\sim$0.5 wt.% CO_2. These fluences allow for clear detection of the implant without substantial radiation damage or self-introduced matrix effects (Burnett et al., 2015). The implant species, matrix density, and energy of implantation determines the depth of the implant. Implantation energies usually vary between 10 and 200 keV (Grob, 2013). We used implant energies of 150 keV in order to place the implant at a depth where contribution from surface contamination would be minimal. A yttrium-doped SiAlON glass with 1.23 wt.% N (Zhang et al., 2003), was also implanted to test whether the nitrogen dose had significant backscattering or unresolved species in the ion beam (Burnett et al., 2015). Thie SiAlON glass was analyzed with a Cs^+ beam as it revealed high yields of NO^- but little or no N^+ implant signal over the counts from the nitrogen-rich glass. The carbon implant dose was checked by comparing the resulting calibration factor with those derived from independently characterized, synthetic carbonated rhyolitic glass standards (Fogel and Rutherford, 1990).

NO^- SIMS depth profiles of implanted samples were completed using a primary beam of Cs^+ accelerated to 10 keV and impacting the sample at $\sim$15keV at a current of $\sim$5nA and rastered over 125 x 125 μm. Negative secondary ions were accelerated to 5 keV and only those with 0 $\pm$ 20 eV excess energy were allowed into the mass spectrometer. A normal-incidence electron gun, aligned using a GaN wafer, compensated

for sample charging (Chen et al., 2013). Only those ions sputtered from a circular area 30 μm in diameter in the center of the raster were allowed into the mass spectrometer. Each cycle of measurement integrated NO^- for 5 seconds and $^{30}Si^+$ for 1 second. The depth profile analysis continued until the NO^- signal decreased to a constant baseline.

Calibration factors for carbon and nitrogen implants, also known as relative sensitivity factors (RSF), are in units of atoms/cm^3 and calculated as:

$$RSF = \frac{\phi N_c I_m t}{d \sum I_i - d I_b N_c} \tag{2.1}$$

where ϕ, fluence (atoms/cm^2), is the dose of the implant, N_C, is the number of cycles required to sample the implant, I_m (c/s) is the intensity of the matrix ion ^{30}Si, t (s) is the integrated time of the ion of nitrogen or carbon measurement, d (cm) is the depth of the implant, $\sum I_i$ (c·cycles/s) is the sum of N^+, NO^-, or C^+ counts from the implant, and I_b (c/s) is the average nitrogen or carbon background under the implant (Wilson et al., 1989). These calibration factors are multiplied by an ion intensity ratio measured on an unknwn to obtain concentrations in atomic density and then converted from atoms/cm^3 to ppm using the following:

$$\frac{RSF \frac{I_i}{I_m} M}{\rho N_A} = [i] \tag{2.2}$$

where I_i/I_m is the ion intensity ratio on the unknown, M is the molar mass of the volatile, ρ is sample density (g/cc), N_A is Avogadro's number, and $[i]$ is the concentration of the volatile. The densities of our rhyolite and SiAlON glasses were measured by an Archimedean scale at Arizona State University and calculated using the equation:

$$p_s = \frac{p_w w_a}{w_a - w_w} \tag{2.3}$$

where p_s is the density of the sample, p_w is the density of water at room temperature, w_a is the weight of the sample in air, and w_w is the weight of the sample in water (e.g. Withers and Behrens, 1999; Richet et al., 2000). Densities and their corresponding errors were determined from four or more replicate measurements (Table 3).

2.1.3 FTIR Measurements

Fourier transform infrared spectroscopy (FTIR) spectra of the rhyolitic glasses were obtained with a Bruker Tensor 27 infrared spectrometer paired with a Bruker Hyperion 2000 microscope at McGill University in Montreal, Canada. A 15 x transmission mode objective lens was used at 4 cm^{-1} spectral resolution. A French curve baseline was fit to absorption peaks at ∼5200 cm^{-1} and ∼4500 cm^{-1}. French curve-determined absorption coefficients, suitable for hydrous, rhyolitic glasses (Withers and Behrens, 1999), were chosen to determine the dissolved H_2O_m and OH contents. Errors associated with these measurements include uncertainty in wafer thickness (± 5 μm) measured with a FTIR stage that was calibrated against a digital micrometer, error in matrix density, reported errors for absorption coefficients, and the heterogeneity between three repetitions. FTIR spectra for the basaltic suite of glasses were collected on a Nicolet Magna 750 at the U.S. Geological Survey in Menlo Park. The ∼5200, ∼4500, and ∼3530 cm^{-1} absorption peaks heights were determined using a French curve baseline fit. Concentrations were calculated using absorption coefficients from (Dixon et al., 1995), and iteratively calculated density (e.g. Luhr, 2001; R. Lange, personal communication). Uncertainties included a 1% error in the wafer thickness, measured by a digital micrometer.

Table 3. Carbon and nitrogen implanted materials and their derived calibration factors

Sample	Species	H_2O (wt.%)[1]	OH (wt.%)	Density (g/cc)	Dose (atoms/cm^2)[2]	Sample ave. RSF (atoms/cc)[3]
Rhyolites						
PCD	$^{14}N^+$	0.21(1)	0.20(1)	2.35(2)	5 x 10^{15}	2.94 ± 0.1 x 10^{24}
PCD	$^{14}N^{16}O^-$	0.21(1)	0.20(1)	2.35(2)	5 x 10^{15}	9.03 ± 4.0 x 10^{22}
PCD	$^{12}C^+$	0.21(1)	0.20(1)	2.35(2)	2.5 x 10^{15}	3.99 ± 0.08 x 10^{23}
M3N	$^{14}N^+$	2.90(9)	1.31(7)	2.36(1)	5 x 10^{15}	8.93 ± 0.3 x 10^{23}
M3N	$^{14}N^{16}O^-$	2.90(9)	1.31(7)	2.36(1)	5 x 10^{15}	1.26 ± 0.1 x 10^{23}
M3N	$^{12}C^+$	2.90(9)	1.31(7)	2.36(1)	2.5 x 10^{15}	3.75 ± 0.08 x 10^{23}
M6N	$^{14}N^+$	5.18(2)	1.17 (11)	2.36(1)	5 x 10^{15}	1.08 ± 0.2 x 10^{24}
M6N	$^{14}N^{16}O^-$	5.18(2)	1.17 (11)	2.36(1)	5 x 10^{15}	9.18 ± 4.0 x 10^{22}
M6N	$^{12}C^+$	5.18(2)	1.17 (11)	2.36(1)	2.5 x 10^{15}	3.83 ± 0.08 x 10^{23}
2	$^{14}N^+$	1.74(1)	n.a.	n.a.	5 x 10^{15}	1.61 ± 0.06 x 10^{24}
4	$^{14}N^+$	3.57(1)	n.a.	n.a.	5 x 10^{15}	8.75 ± 0.4 x 10^{23}
6	$^{14}N^+$	4.53(1)	n.a.	n.a.	5 x 10^{15}	8.82 ± 0.5 x 10^{23}
Basalts						
z19	$^{14}N^+$	1.6(8)	1.31(7)	n.a.	5 x 10^{15}	9.89 ± 0.4 x 10^{23}
z19	$^{14}N^{16}O^-$	1.6(8)	1.31(7)	n.a.	5 x 10^{15}	4.94 ± 1.0 x 10^{22}
x103	$^{14}N^+$	2.8(1)	1.72(9)	n.a.	5x10^{15}	1.25 ± 0.05 x10^{24}
x103	$^{14}N^{16}O^-$	2.8(1)	1.71(9)	n.a.	5 x 10^{15}	5.6 ± 0.7 x 10^{22}
x61	$^{14}N^+$	4.75(24)	2.06(10)	n.a.	5 x 10^{15}	1.73 ± 0.06 x 10^{24}
x61	$^{14}N^{16}O^-$	4.75(24)	2.06(10)	n.a.	5 x 10^{15}	1.16 ± 0.04 x 10^{23}
x107	$^{14}N^+$	5.71(29)	2.13(11)	n.a.	5 x 10^{15}	1.83 ± 0.07 x 10^{24}
x107	$^{14}N^{16}O^-$	5.71(29)	2.13(11)	n.a.	5 x 10^{15}	1.09 ± 0.04 x 10^{23}
YSiAlON						
NO	$^{14}N^{16}O^-$	n.a.	n.a.	3.48(2)	5.57 ± 0.6 x 10^{15}**	6.18 ± 0.6 x 10^{21}*

Errors are 1 sigma, in parentheses or otherwise [1] Total water is OH + molecular H_2O [2]N dose was verified by implantation into YSiAlON; carbon dose was verified using standards [3] RSF errors are 1 sigma *RSF was calculated using Eq. 2.2 **Dose was calculated using Eq. 2.1 and the derived RSF.

2.2 Results

2.2.1 Nitrogen Implants

Backscattering or unresolved species in the implanted ion beam have the potential to reduce the concentrations of implanted species. In order to determine if these error-inducing processes were significant, a SiAlON glass with 1.23 wt.% N (Zhang et al., 2003) was also implanted. Using this bulk-analyzed nitrogen content for $[i]$ in Equation 2.2 allows for the determination of the SiAlON RSF. Entering this RSF into Equation 2.1 results in a calculated implant flux equal within error to the target dose of 5 x 10^{15} atoms/cm^2 (Table 3). Therefore, no correction to the implant dose was necessary.

The sensitivities resulting from using different secondary species can be quantified by determining useful yields, or the number of ions detected per nitrogen atom removed from the sample (e.g. Hervig et al., 2006). Depth profile analysis of the N^+ species, which requires only low MRP, returns greater useful yields than do high MRP analyses of the NO^- species (Fig. 3). While the sensitivity of NO^- is lower, a Cs^+ beam of 5 nA sputtered ~4 x faster than that of a O^- primary beam of 20 nA. This fast sputtering releases more nitrogen atoms that can potentially be ionized. Therefore, while the useful yield will remain lower for the NO^- species at all currents, the counts that can be obtained from NO^- and N^+ may be similar under high Cs^+ current. This may be particularly true for basalts and relatively dry rhyolites where the difference in useful yields between NO^- and N^+ are often less than an order of magnitude (Fig. 3).

The low yields of NO^- for hydrous rhyolites and the larger errors (>10% SE) in NO^- RSF (Table 3), caused by inadequate electron gun charge compensation for a

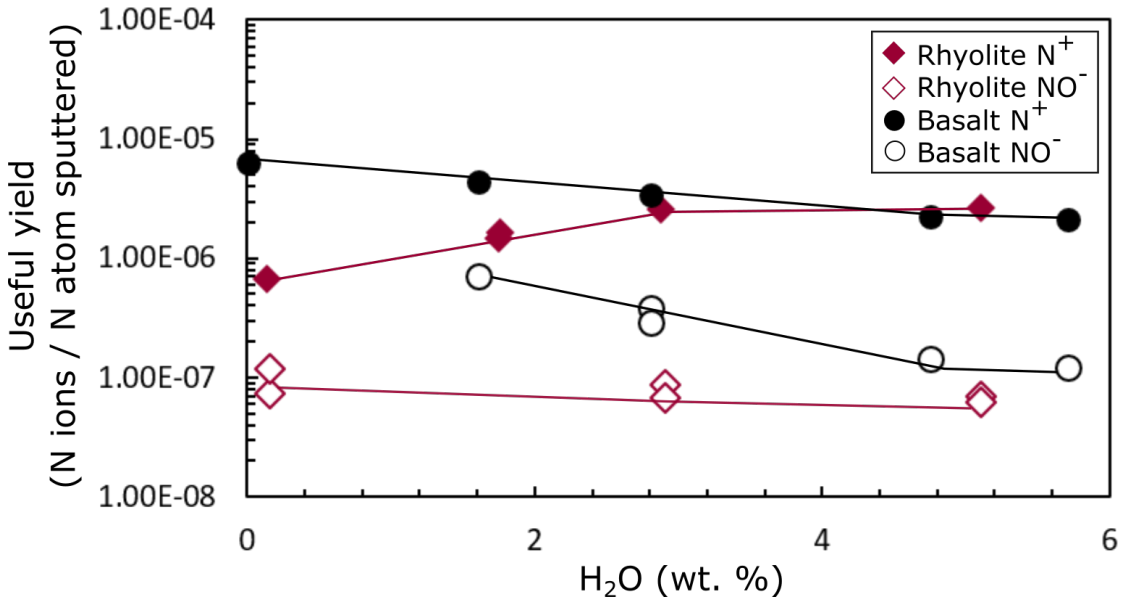

Figure 3. N^+ and NO^- useful yields in rhyolitic and basaltic glasses. Useful yields were calculated by depth profiling through implants containing a known number of atoms. Depth profiles of any one species and matrix pair were completed in the same analysis session. However, as four different sessions are represented here, small changes in MRP or primary beam alignment may result in small changes in the useful yield of one species relative to another. Errors are smaller than symbols.

large raster, led us to utilize the N^+ species for all analyses of non-implanted samples. While analyses of N^+ yield consistent RSF, with <10% SE per sample over 1 year (Table 3), the useful yields record systematic changes with water content (Fig. 3). This can also be observed in figure 4, where the N^+ species was monitored during depth profiles of dry and hydrous rhyolitic glass implants. Despite the analytical conditions and the dose of the implant being the same, the N^+ signal from the hydrous glass is significantly more intense than the 0.21 wt.% H_2O sample. In addition, the peak of the implant is reached in a shorter analysis time, despite using the same primary current. Clearly, both the sputtering rate and the probability of nitrogen ion formation are enhanced in rhyolites when H_2O is added. This translates into hydrous rhyolites having N^+ calibration factors that are >3 times lower than those for the

dry starting material. Conversely, basaltic calibration factors are positively correlated with water content, with the 5.71 wt.% H_2O sample showing a ~2 x greater N^+ RSF than the dry natural East Pacific Rise sample. Hydrous basaltic NO^- calibration factors are ~2.4 x greater than dry samples, wherease rhyolitic calibrations are nearly equal for variably hydrated glasses (Fig. 5).

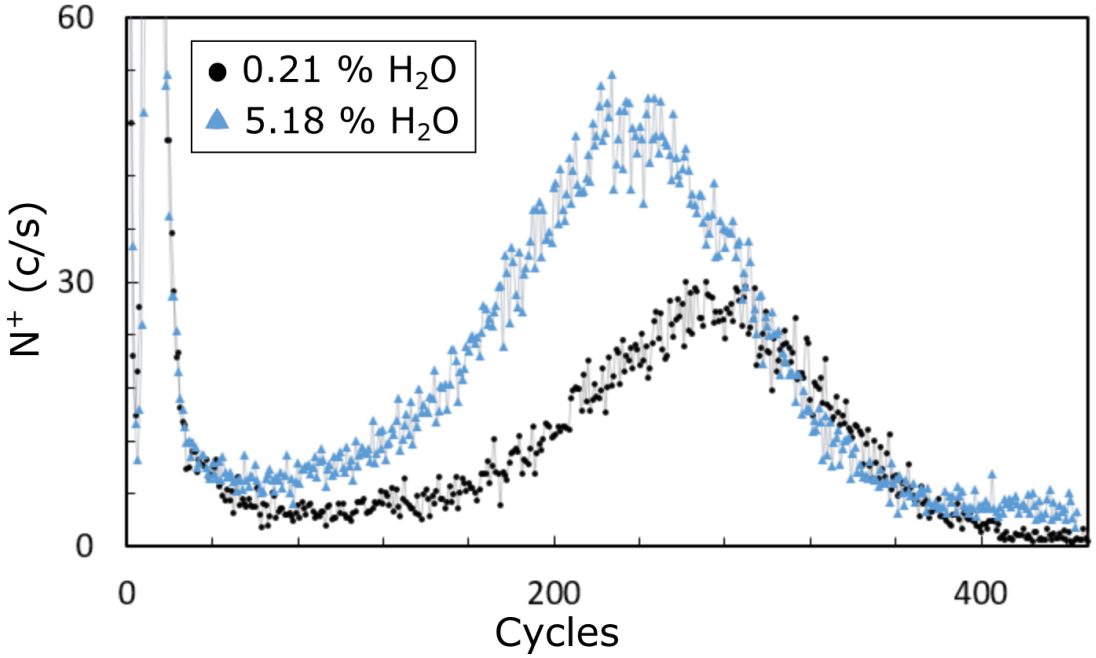

Figure 4. N^+ depth profiles into implanted rhyolites. Both profiles were obtained in the same analytical session using the same analytical parameters. The peak offset is caused by faster sputtering of hydrous glass. The higher intensity counts per second (c/s) for the blue peak demonstrates the greater yield of nitrogen ions from a hydrous glass. The average $^{30}Si^+$ intensities for the dry and hydrous glasses (not shown) are near equal, at 2.39 x 10^5 and 1.92 x 10^5 c/s respectively.

2.2.2 Carbon Implants

The flux of the carbon implant was verified by comparing concentrations derived from our calculated RSF and from infrared spectroscopy-characterized rhyolites (Fogel

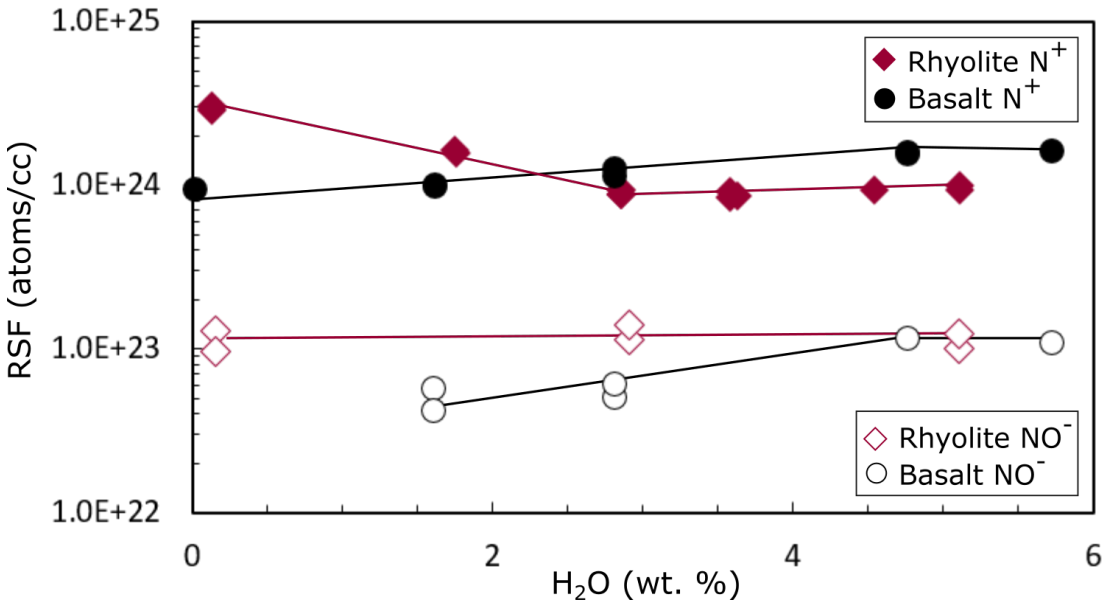

Figure 5. N^+ and NO^- RSF calibration factors for rhyolitic and basaltic glasses. Hydrous rhyolitic glasses show higher sensitivity to N^+ and therefore, a lower RSF, whereas the opposite is observed for basaltic glasses. Hydrous basaltic glasses also show a lower sensitivity to N^+ and therefore, a higher RSF. The non-flat best fit lines are linear regressions and have R^2 >0.98. When RSF is within 10% SE, they are assumed to be equal. Error bars are smaller than the symbols.

and Rutherford, 1990; Fig. 6). We did not detect an effect of water content on the C^+ calibration in rhyolites and derived a RSF calibration factor of 3.85 ± 0.08 x 10^{23} atoms/cc (Table 3). C^- and basaltic C^+ calibrations are not reported here.

2.2.3 Background Subtraction

A non-trivial complication that arises during volatile analyses is blank subtraction. Analysis of the low H_2O natural rhyolite, PCD, shows unreasonably high apparent background compared to hydrous glasses when appropriate calibration factors are used. This observation can be caused by the low sputtering rate of the dry glasses. We observe that hydrous rhyolite and basaltic glasses sputter ≤1.3 x and ≤1.05 x faster

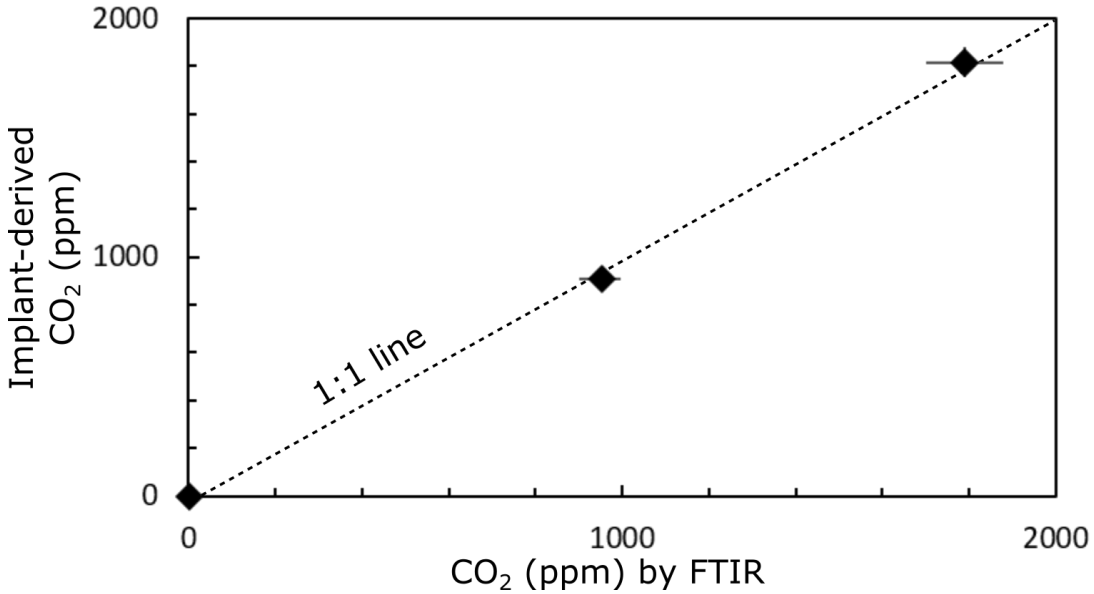

Figure 6. Verification of carbon implant dose using CO_2 rhyolite standards characterized by infrared spectroscopy and implant-derived SIMS calibrations of the same samples. The data fall within error of the 1:1 line, which suggests that the implanted dose was correctly estimated.

under O^- bombardment than their dry counterparts (Fig. 7). A similar trend is found in data tabulated by Hauri et al. (2006), which show that hydrous basaltic glasses have sputter yields, and thus sputter rates, ∼1.4 x larger than their anhydrous counterparts under a Cs^+ primary beam. We tested the effect of sputter rate on background levels by monitoring background ion intensity ratios on the PCD rhyolite under various sputter rates, determined by raster size (Fig. 8). The results demonstrate that background N and CO_2 decrease exponentially with the log of sputter rate. As sputter rate is increased, background is drowned out by the increasing flux of sample-derived ions. Therefore, as sputter rate approaches infinity, the remaining signal reflects the true concentration of the matrix. The least square regressions of linearized exponential fits return y intercepts of ∼0.0030 ± 1.9 ppm N and ∼0.0027 ± 7.0 ppm CO_2. Therefore, the natural rhyolitic obsidian, PCD, represents a reasonable nitrogen and CO_2 blank

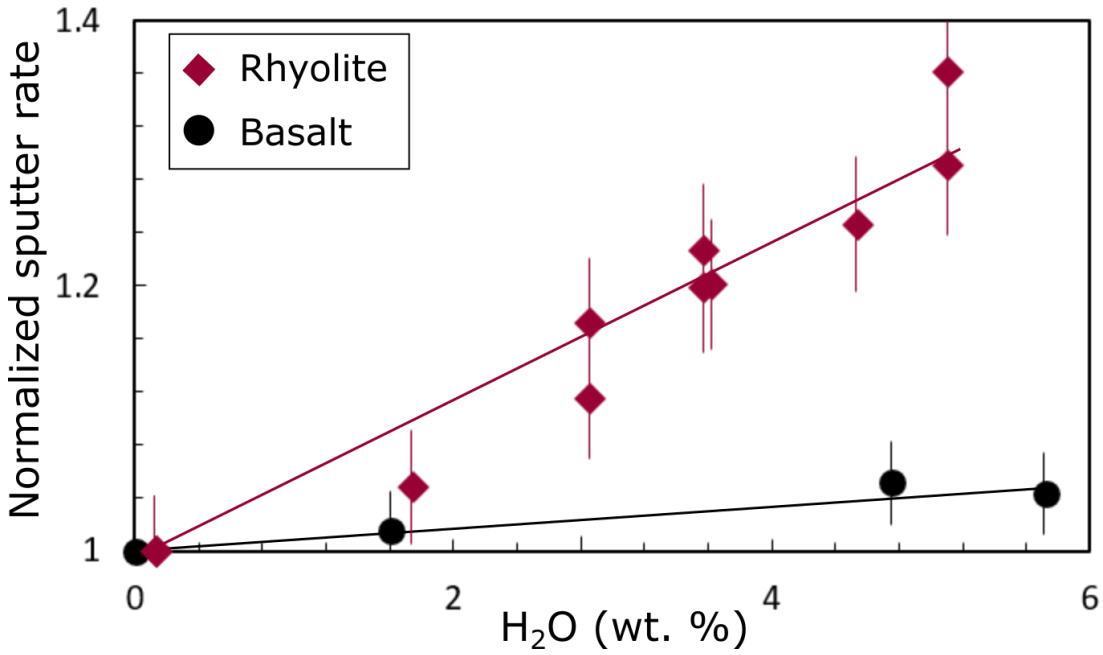

Figure 7. Sputter rate of experimentally-hydrated glasses normalized to the primary current and the the sputter rate of the low water PCD natural rhyolite or the East Pacific Rise natural basalt. Normalization to the primary current allows easier comparison between different analytical sessions, and normalization to the dry glasses allow for the effect of water on sputter rate to be quantified. Typical sputter rates for PCD are 3.65 $\pm$ 0.2 x 10^{-6} μm s^{-1} nA^{-1} and for EPR are 3.27 $\pm$ 0.4 x $10^{-6}\mu$m s^{-1} nA^{-1}. The linear fits have a R^2 of 0.95 for rhyolites and a R^2 of 0.51 for basalts.

for this study. We note that a similar method has been used to quantify a hydrogen blank (Stephant et al., 2014). In addition, the analysis of the PCD obsidian with a 75 micron raster and a 15 micron analyzed diameter shows near equal or greater volatile intensity ratios as an analysis in the same crater using a 30 micron analyzed diameter. This demonstrates that selecting an analyzed diameter $\leq$2/5 the size of the raster will not significantly increase crater wall contamination.

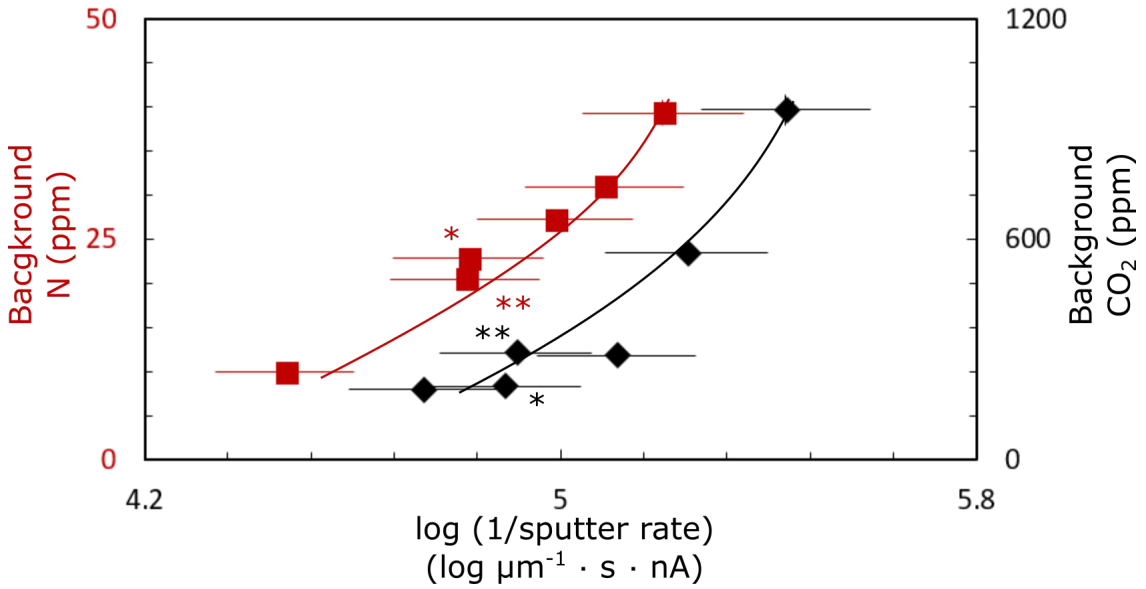

Figure 8. Current-normalized sputter rates for PCD natural rhyolite and corresponding CO_2 and N backgrounds. Sputter rates were determined under a variety of different raster sizes, with smaller raster sizes promoting faster sputtering. ** indicates 75 x 75 μm raster and 15 μm diameter analyzed area and * indicates 75 x 75 μm and 30 μm diameter analyzed area. The exponential fits have a R^2 of 0.98 for nitrogen and a R^2 of 0.90 for CO_2. Some 1 sigma errors are smaller than the symbol.

2.2.4 Density of Glasses

While the addition of water generally decreases glass density (Ardia et al., 2014), our Archimedean estimates show that the 0.21 to 5.18 wt.% H_2O rhyolitic glasses have values equal within error (Table 3). Since density is also a function of quench rate (Withers and Behrens, 1999), the high densities of the experimental glasses are most likely a reflection of the slow quench rates (Ardia et al., 2014) related to an internally heated pressure vessel. Our density measurement of the natural rhyolite, PCD, agrees with Newman et al. (1986) within <1 g/cc.

Chapter 3

APPLICATION TO MELT INCLUSIONS

3.1 Melt Inclusion Preparation and Analytical Methodology

Quartz crystals containing melt inclusions from the Bishop Tuff, the Huckleberry Ridge Tuff, and the Taupo Volcanic center, were examined using transmitted light under immersion oil (n = 1.492). Only those crystals containing melt inclusions larger than 50 μm and without visible cracks and bubbles were selected for study. The crystals were then mounted in Crystalbond^{TM}, and polished to expose the inclusion on one side. After removal of the Crystalbond^{TM} with acetone, they were pressed into indium contained within 1-inch diameter aluminum disks.

Two suites of early erupted Bishop Tuff samples that were previously analyzed for H_2O and CO_2 by FTIR were also analyzed for nitrogen. For both suites, the Beer-Lambert law was used to convert absorbances to total H_2O and CO_2 concentration. The first suite of doubly-polished inclusions (Bishop F1a-FTIR) were analyzed on a Nicolet Magna 750 at the U.S. Geological Survey in Menlo Park. CO_2 content was determined using the peak at 2350 cm^{-1}, an absorption coefficient (ϵ) of 1213 $\pm$ 16 L $\cdot$ cm^{-1} $\cdot$ mol^{-1} (Behrens et al., 2004), and a constant density of 2.35 g/cc. Total H_2O was calculated after Zhang et al. (1997) using peaks at 5230 and 4520 cm^{-1}. Thickness of each doubly polished inclusion was determined with a pin micrometer with a error of $\sim$2 μm (K. Befus, personal communication). The second suite of FTIR-analyzed inclusions (Bishop F1b-FTIR) were analyzed on a Thermo Nicolet Nexus 670 FTIR spectrometer interfaced with a Continuum IR microscope at University of Oregon.

ρ and ϵ were calculated iteratively using $\rho = 2350 - 12.6 \cdot H_2O$ (Skirius, 1990) and $\epsilon = 80 - 1.36 \cdot H_2O$ (Leschik et al., 2004), with H_2O in wt.%. All wafers >80 μm thick required H_2O absorbance to be measured on the 5230 and 4520 cm^{-1} peaks (after Zhang et al., 1997), whereas the 3570 cm^{-1} peak was used for wafers 30 - 70 μm thick. Thickness was measured using the reflectance interference fringe and a digital micrometer, which show agreement within 4 μm (Myers et al., in press).

SIMS analytical methods for MI were identical to those used for the implants, but with a smaller raster of 75 x 75 μm and a pre-sputter of at least 11 minutes. Each melt inclusion mount included chips of PCD, M3N, and M6N to serve as H_2O standards, and CO_2 and nitrogen blanks (Table 3; see section 2.2.3). We used the least squares regressions between water content and the RSF for nitrogen to derive calibration factors for individual inclusions with total water contents below 2.90 wt.% (Fig. 5). Errors associated with each individual melt inclusion RSF were derived from the linear regression. For inclusions with >2.90 wt.% H_2O, we used the average RSF from our hydrous standards (9.59 $\pm$ 0.4 x 10^{23} atoms/cc). The average carbon implant-derived RSF, 3.85 $\pm$ 0.05 x 10^{23} atoms/cc, was used to quantify CO_2 in melt inclusions. As conversion from atoms/cc to ppm concentration requires a density estimate, we used the partial molar volumes of various oxides (Luhr, 2001), the determined water content of each inclusion, and the major element compositions of quartz-hosted melt inclusions from the Bishop (Dunbar and Hervig, 1992), Oruanui eruption (Liu et al., 2006), Huckleberry (Myers et al., in press), and Oruanui (Lowe et al., 2008). We assume a large error of 0.05 g/cc for each inclusion, which accounts for the uncertainity in these major element and partial molar volume estimations (Luhr, 2001).

Table 4. Steps and figures utilized to determine nitrogen in melt inclusions

Step	Description	Figures
	Before inclusion analysis session, we established...	
1	The effect of H_2O on PCD-normalized sputter rates	Fig. 7
2	The effect of sputter rate on background $^{14}N^+/^{30}Si^+$	Fig. 8
	During inclusion session, we established...	
3	Sputter rate of the blank	–
4	$^{14}N^+/^{30}Si^+$ of the blank	–
5	H_2O contents of inclusions	–
	We then converted...	
6	Inclusion H_2O into normalized sputter rate	Fig. 7
7	Normalized sputter rate into inclusion sputter rate using that session's PCD sputter rate	–
8	Inclusion sputter rate into background $^{14}N^+/^{30}Si^+$ corrected for the session's PCD $^{14}N^+/^{30}Si^+$	Fig. 8*
9	Inclusion's $^{14}N^+/^{30}Si^+$ minus background into N (ppm) with appropriate calibration	Fig. 5

*Figure 8 shows concentration of background species, whereas the above process requires an ion intensity ratio vs. sputter rate exponential fit. Both graphs have a similar exponential fit.

Sputter rate varies between sessions because of variations in primary beam density. Similarly, the background for a specific sputter rate will vary based on the vacuum quality. Therefore, each melt inclusion analytical session involved a calculation of sputter rate on H-poor, CO_2 and N-free PCD and the associated $N^+/^{30}Si^+$ ion intensity ratio. Using the established correlation between H_2O and normalized sputter rate (Fig. 7), we calculated the normalized sputter rate for each inclusion based on its H_2O contents. We then calculated each inclusion's sputter rate by multiplying the normalized rate to that session's PCD sputter rate. Then with the pre-established correlation between sputter rate and ion intensity ratio (Fig. 8), corrected for the day's vacuum using the PCD $N^+/^{30}Si^+$ ratio, each melt inclusion's sputter rate was transformed into a background ion intensity ratio. This process is described in Table

4. The error associated with the melt inclusion sputter rate was calculated using a least squares regression and propagated to include the uncertainty of the sputter rate and ion intensity ratio of PCD. A similar process was completed for CO_2 background measurements.

3.2 Results

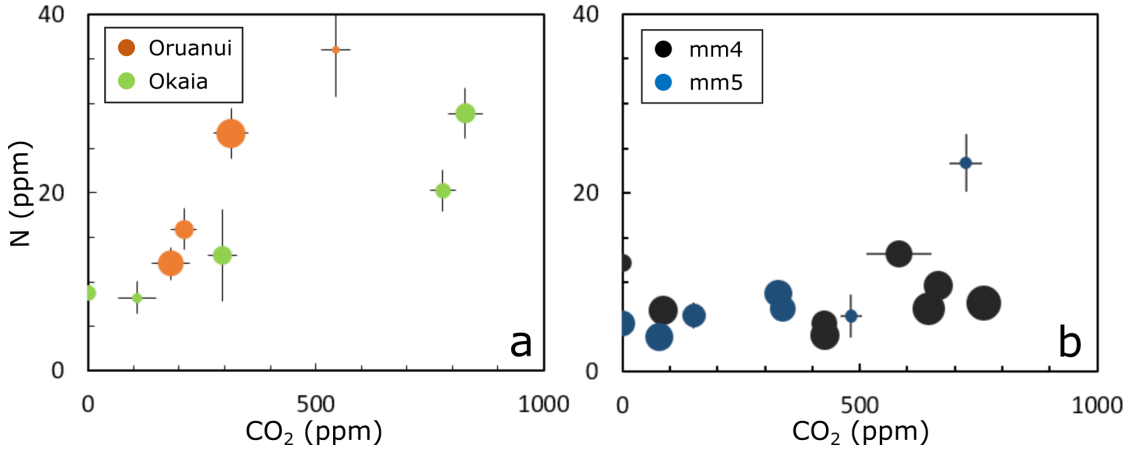

Figure 9. H_2O, CO_2, and N contents of the Taupo Volcanic Center and Huckleberry Ridge Tuff eruptions. **a** Volatile contents of the Oruanui and Okaia eruptions with higher H_2O contents indicated by larger symbols (1.59-5.78 wt.% H_2O). **b** Volatile contents of the mm4 and mm5 samples of the Huckleberry Ridge Tuff with higher H_2O contents indicated by larger symbols (1.20-3.28 wt.% H_2O.)

Melt inclusions from all three rhyolitic centers have nitrogen contents $\leq$45 ppm and show a positive correlation between nitrogen and CO_2 (Figs. 9, 10). No consistent correlation between N and H_2O was discerned (Fig. 11). Samples from both the Okaia and Oruanui eruptions, have high maximum contents of $\sim$35 ppm, whereas the majority of the Huckleberry Ridge Tuff inclusions show lower nitrogen concentrations (Fig. 9). Melt inclusions from various deposits within the Bishop Tuff show a gradient

from high nitrogen in the early erupted material to low nitrogen in the later erupted material (Fig. 10).

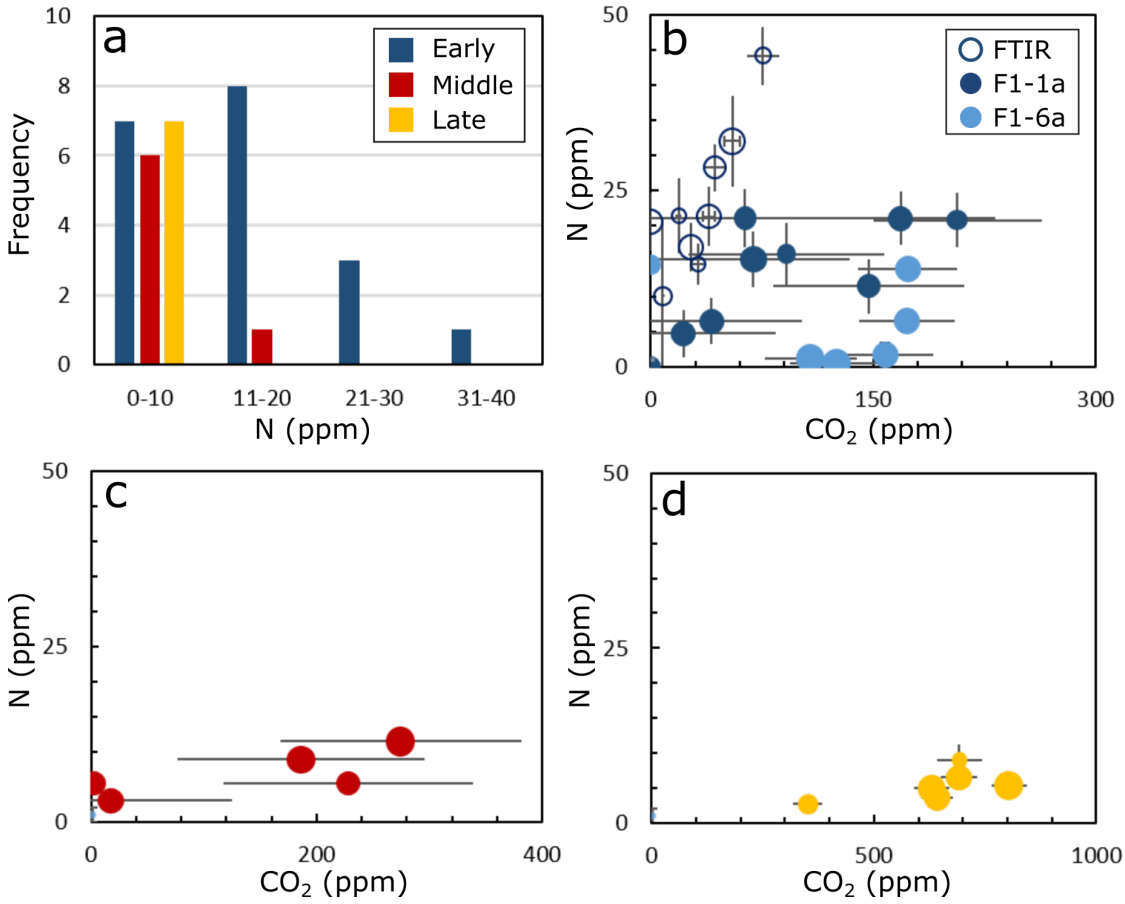

Figure 10. H_2O, CO_2, and N contents in the early, middle, and late erupted Bishop melt inclusions. **a** Nitrogen contents in the early, middle, and late-erupted deposits of the Bishop Tuff. **b** Volatile contents of the early erupted melt inclusions. "FTIR" indicates those inclusions with FTIR-determined CO_2 and H_2O and SIMS-determined nitrogen. H_2O ranges from 4.06-5.45 for f1-1a, 3.97-5.39 for f1-6a, and 3.48-5.70 wt.% H_2O for FTIR-analyzed inclusions, with higher concentrations indicated by larger symbols. **c, d** CO_2 and N contents measured by SIMS of the middle (2.86-3.75 wt.% H_2O) and late erupted Bishop Tuff inclusions (2.08-3.78 wt.% H_2O). All errors are 1 sigma.

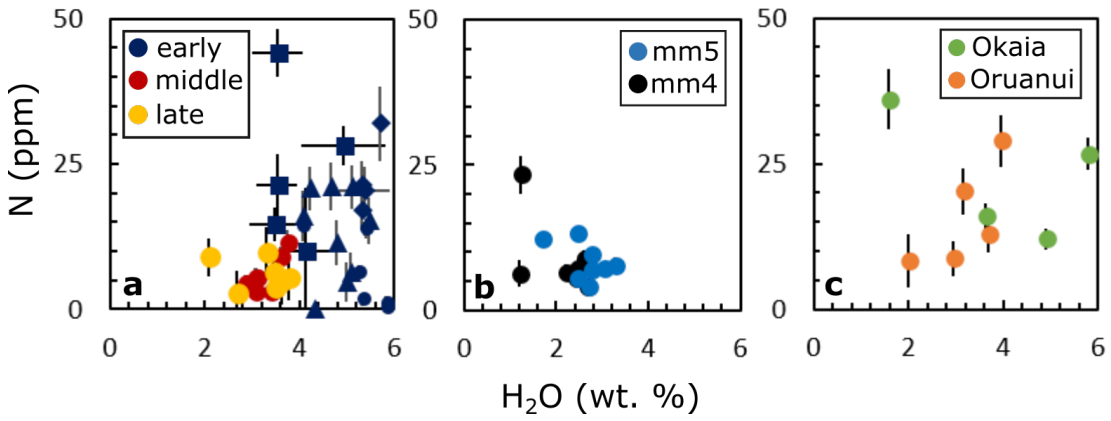

Figure 11. H_2O and N contents of the all three volcanic centers. **a** The Bishop Tuff is colored according to eruption sequence, squares correspond to F1a-FTIR, diamonds to F1b-FTIR, triangles to F1-1a, and blue circles to F1-6a. **b** Samples mm4 and mm5 of the Huckleberry Ridge Tuff. **c** Okaia and Oruanui material of the Taupo Volcanic Center.

Due to the relatively low sputtering rate of an oxygen primary beam, our melt inclusion analyses were plagued with high levels of carbon contamination. This carbon background is sourced from memory effects of the volatile rich surface, and vacuum contaminants from pump oil and prior samples. These high contaminant levels may have resulted in inaccurate absolute concentrations due to large background subtractions. Nevertheless, the correlation between CO_2 and nitrogen is substantiated by the independently determined CO_2 in those inclusions analyzed by FTIR (Fig. 10b).

Chapter 4

DISCUSSION

4.1 The Effect of Water on N^+ Yields

The increase in water content of rhyolitic glass from 0.21 to 2.90 wt% is correlated with an increase in N^+ sensitivity by a factor of ∼3 and a decrease in sensitivity to NO^- by a factor of ∼1.4. A change from 1.6 to 4.75 wt.% H_2O in basaltic glasses shows a factor of ∼2.2 decrease in N^+ sensitivity and a factor of ∼2.4 decrease in NO^- sensitivity. While it may not be surprising that wt.% variation in water content creates matrix effects, the quantification of this effect and the range of water contents over which it occurs has not been systematically reported.

The reason behind these changes in calibration is more difficult to pinpoint. Sputter rate controls the concentration of primary beam added to the matrix, and may therefore create changes in ion yield. However, sputter rate increases linearly (Fig. 7), so it cannot be the sole source of the calibration changes that only occur at <3 wt.% H_2O for rhyolites and <5 wt.% H_2O for basalts. Infrared spectroscopy of hydrous glasses shows that hydrogen is dissolved as two different species (e.g. Newman et al., 1986), OH ions and molecular H_2O. Examining the abundance of OH species shows a strong linear relation with the useful yield of nitrogen ions (Fig. 12). This suggests that the presence of OH in a silicate glass affects the probability of forming nitrogen ions, while the presence of molecular H_2O does not. If this is the case, the magnitude and range of calibration change would also be dependent on the temperature at which the glasses were quenched.

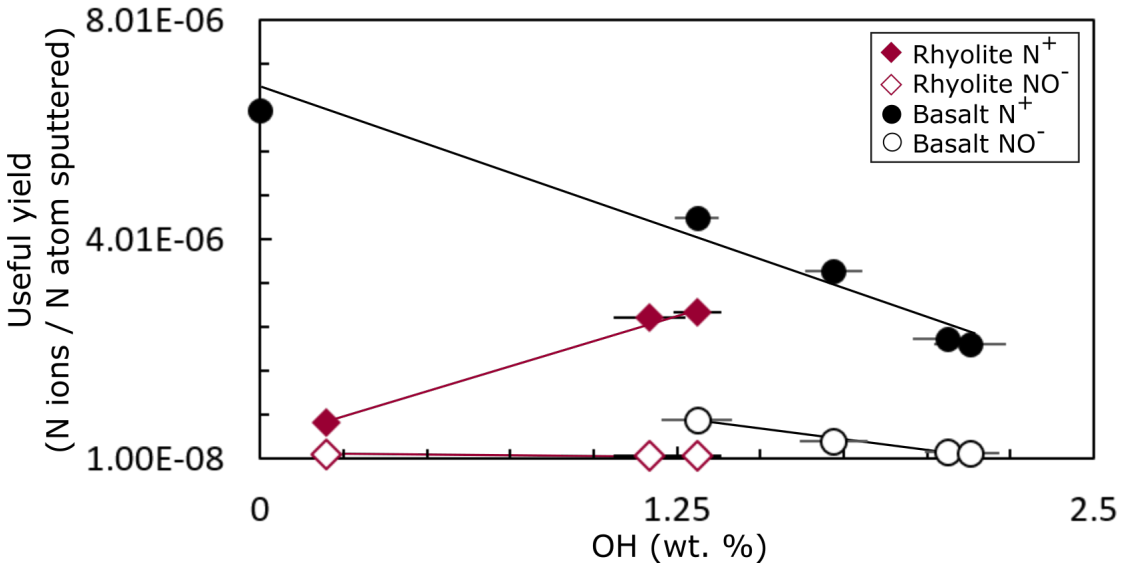

Figure 12. OH versus useful yield of nitrogen in rhyolitic and basaltic glasses for the N^+ and NO^- species. Useful yields were determined in one analytical session for matrix/species pairs. Errors are 1 sigma. R^2 for the N^+ species is 0.97 for basalts and 0.99 for rhyolites. R^2 for the NO^- species is 0.98 for basalts and 0.94 for rhyolites.

In SIMS, two processes must occur during sputtering to detect a signal: 1) the atom must be ejected from the surface, and 2) that atom must be ionized. Invoking a role of hydrogen species in a glass to explain the changes in ion yield goes against our initial thoughts concerning sputtering. Chemical bond strengths within a silicate glass of ~1-5 eV are over four orders of magnitude weaker than the energy of a 12.5 keV O^- primary ion beam striking a sample held at 9 kV. Therefore, it is normally assumed that the bonds affected by this bombardment would be completely rearranged. However, energy spectra of hydrous, diatomic molecular ions often show high energy tails (Schauer and Williams, 1990). This suggests that while sputtering must rearrange surface atoms, hydride ions either re-form after primary ion impacts or are not destroyed as efficiently as other molecules under high energy bombardment.

Sputtering with oxygen is a well-known technique to enhance yields of positive secondary ions. One tentative explanation for this is that the oxygen beam creates a

more ionic surface (Franzreb et al., 2004). Similarly, if the addition of hydrogen into a silicate network forces an atom of interest into an ionic environment, then we need only eject it to have a chance to detect it. The dissolution of H_2O into a rhyolite glass at low total water contents, breaks bridging oxygen bonds, and increases the concentrations of non-bridging and free oxygen atoms (Mysen et al., 1980). We speculate that the negative charges on these oxygen atoms increase the ionic environment of the matrix and may be responsible for holding nitrogen in ionic bonds after the N_2 covalent bonds are destroyed by sputtering. These weak ionic bonds then increase the efficiency of N^+ formation and detection. Our observations also show a negative trend for basalts (Fig. 12). In this case, we speculate that a high concentration of network modifiers in the anhydrous mafic glass force the presence of many non-bridging oxygen atoms (Mysen et al., 1980). This high ionic environment may be responsible for the high N^+ and NO^- useful yields of dry basaltic glasses. The dissolution of hydrogen at low total water contents creates OH bonds with some non-bridging ions (Mysen et al., 1980), reducing the ionic environment, and potentially leaving nitrogen to reform covalently bonded N_2 molecules after sputtering. This results in a lower potential to form N^+ and NO^- ions. For both matrices, the ionic environment, and therefore, ionic yields, remain constant after saturation of OH, as molecular H_2O dissolves within the free spaces of the silicate network (Nuccio and Paonita, 2000).

While we cannot unambiguously determine the cause of the correlation between OH and useful yield, such a change in calibration factor for nitrogen secondary ion species (Fig. 5) indicates that if nominally dry glasses are used as standards, subsequent analyses of hydrated glasses will give concentrations that are up to $\sim$3 x different than analyzes using correct water-matched standards. However, calibrations based on highly hydrated glass to study other very hydrated glasses (e.g. Li et al., 2015)

should be more accurate. Ion yields for other elements may also be dependent on H_2O content or speciation (e.g., Hervig et al., 2009). Such effects are difficult to show unless one has a suite of glasses with a range of H_2O contents and identical amounts of the element of interest. Thus, implantation is an ideal and unambiguous method to substantiate such matrix effects.

4.2 Volatiles in Melt Inclusions

The measurement of nitrogen in melt inclusions reaffirm the low, but measurable, solubility of N_2 in rhyolitic systems. The low maximum measured nitrogen concentrations of the Huckleberry Ridge Tuff compared to the other three eruptions, suggests that either the intraplate tectonic environment provides lower initial magmatic nitrogen contents than arc related settings, or that more extensive degassing occurred prior to inclusion entrapment.

As the nitrogen yields for our inclusions are too low to obtain nitrogen isotope ratios, the origin of the nitrogen in our melt inclusions remain enigmatic. The nitrogen sources in these systems may be mantle, slab, or crustal. Past research has supported little to no country rock incorporation in the Bishop system (Hildreth and Wilson, 2007). However, the nitrogen gradient opposes the mantle-derived CO_2 gradient with depth, and may therefore, support the idea that at least some of the nitrogen is crustally-derived. Sedimentary and metamorphic rocks such as schists and shales may contain ∼500 ppm and ∼860 ppm nitrogen as NH_4^+ (Johnson and Goldblatt, 2015), so small levels of roof rock incorporation could be responsible for supplying the nitrogen found in these inclusions. Another explanation for the apparent nitrogen gradient may be the reduced N_2 solubility in CO_2-rich rhyolitic melts. Nuccio and Paonita

(2000) point out that molecular CO_2 dissolves within the spaces of a rhyolitic silicate network, leading to lower solubility of other inert gases. Therefore, the low nitrogen concentrations in the later, CO_2-rich Bishop Tuff deposits may be reflecting a lower N_2 solubility than the H_2O-rich early erupted magma.

An observed correlation between nitrogen and carbon dioxide in melt inclusions (Fig. 10) could be the result of post or pre-entrapment exsolution. Kesson and Holloway (1974) presented measurements of the nitrogen content of albite glass in experiments where the partial pressure of N_2 was known. With 40 ppm dissolved nitrogen, the partial pressure of nitrogen at total pressures of 2.1 to 2.9 kbar is <300 bars. These partial pressures suggest that vapor bubbles in melt inclusions might contain significant amounts of nitrogen as well as CO_2. However, as we avoided inclusions with bubbles, this is not the cause of our trend.

Another mechanism that would cause this correlation is pre-entrapment volatile exsolution. Since isobaric, gas-saturated crystallization is often invoked in large, rhyolitic systems (Wallace et al., 1999), the observed correlation between CO_2 and nitrogen is most simply explained as crystals progressively entrapping melt representing variable amounts of volatile degassing. Therefore, the best estimates of initial nitrogen concentrations are the maximum for each locality. Because of the possibility of a multi-species vapor phase during melt inclusion entrapment, we must assume these are minimum estimates of initial dissolved nitrogen.

Using our maximum measured nitrogen contents, published dense rock equivalents (DRE) volumes, and a melt density of 2450 kg/m^3, which is representative of large silicic eruptions (Mason et al., 2004), we can estimate the minimum erupted mass of nitrogen. Taking an average 40 ppm nitrogen for the upper Bishop, 15 ppm for the middle Bishop, and 10 ppm for the late Bishop, which have dense rock equivalents (DRE) of

200 km^3, 400 km^3 and ~50 km^3 (Wallace et al., 1999), we can then estimate that the Bishop Tuff released >3.6 x 10^{13} g of nitrogen. With the equation $M = log(m) - 7$, where M is the magnitude of the event and m is kg of erupted mass, we calculate that the Bishop Tuff was a M8.2 eruption, which has an occurrence rate of ~0.2 Ma (Mason et al., 2004). Assuming all M8.2 eruptions have similar nitrogen concentrations, we can calculate a yearly average of 1.7 x 10^8 g of nitrogen. Similarly, if we use the maximum nitrogen content of 24 ppm in the 2200 km^2 DRE Huckleberry Ridge Tuff (Christiansen, 1984, 2001), we calculate that 1.3 x 10^{14} g of nitrogen were released during this 8.8M eruption. Assuming similar eruptions occur every 5 Ma (Mason et al., 2004), then the yearly flux from Huckleberry-type eruptions is 2.8 x 10^7 g of nitrogen. Likewise, the 1.5 km^3, M5.6 Okaia eruption released 1.1 x 10^{11} g of nitrogen, or 4.4 x 10^9 g of nitrogen per year, and the 530 km^3, M8.1 Oruanui eruption released 4.7 x 10^{13} g of nitrogen, or 3.5 x 10^8 g of nitrogen per year (Wilson and Charlier, 2009).

Recent arguments have postulated that biological fixing of N_2 into reactive nitrogen and the denitrification and anammoxization of the nitrogen back to atmospheric N_2 is in a delicate mass balance (Canfield et al., 2010) with continental numbers ranging around 1 x 10^{14} g of nitrogen per year (Galloway, 1998). If that is correct, and the nitrogen in our inclusions was sourced from the crustal reservoir, devolatilization of crustal nitrogen to the atmosphere may be significant when compared to the near equilibrium of biological processes. However, our numbers suggest that even if fixation was only slightly favored over denitrification and anammoxization in the past, volcanic devolatilization would not be significant enough to inhibit crustal nitrogen sequestration.

If the greater part of the nitrogen in these inclusions instead originated in the mantle, we can relate our numbers to MORB and arc flux estimates. The estimate of 6.16 x 10^{10} g of nitrogen released by MORBS and arcs yearly (Fischer, 2008) is 8 x greater than the yearly flux from Okaia-type eruptions and >18 x greater than the yearly flux from the larger eruptions. This leads to the conclusion that if some rhyolitic eruptions tap mantle nitrogen reservoirs, small eruptions may slightly increase the yearly mantle to atmosphere flux, but larger ones are relatively insignificant.

Finally, if we assume all M8 and M9 eruptions (10^{15} and 10^{16} kg) have average occurrence rates of 11.7 M8 events and 0.75 M9 events per Ma (Mason et al., 2004), and contain, on average, 40 ppm nitrogen, we derive an estimate of 1.7 x 10^{18} g nitrogen transferred from the mantle and/crust to the atmosphere in 3.5 Ga years. This estimate is valid as many $\geq$ M8 eruptions are silicic and the calculated occurrence rates do not take into account flood basalts (Mason et al., 2004). However, this estimate is more than three orders of magnitude smaller than the current atmospheric reservoir. So, while large rhyolitic eruptions may ephemerally increase the yearly atmospheric nitrogen flux, they have only contributed a small fraction to buildup and maintenance of the atmospheric nitrogen levels.

4.3 Conclusion

The measurement of useful yields in rhyolitic and basaltic glasses demonstrate that the N^+ signal has a greater useful yield than the NO^- species. However, under a rapidly sputtering Cs^+ primary beam (>5 nA) the resultant counts of NO^- and N^+ are near equal for basalts and dry rhyolites. The calibrations for both of these signals are dependent on the H_2O content of the matrix and are linearly correlated with

OH content. Applying implant-derived calibrations to quartz-hosted melt inclusions determines that the Bishop Tuff, Huckleberry Ridge Tuff, and two eruptions from the Taupo Volcanic Center have measurable nitrogen contents of $\leq$45 ppm and that nitrogen is positively correlated to CO_2. These concentrations, while initial magmatic minimums, suggest that these rhyolitic eruptions only ephemerally increase the yearly mantle/crust to atmosphere fluxes.

4.4 Future analyses

Any future SIMS analyses of C-poor, variably-hydrated silicate glasses may use either the NO^- or N^+ secondary ion species. If the N^+ ion is selected, the analyst must 1) use matrix-matched standards with appropriate water contents and 2) quantify the effect of water content on background intensities. Because background is exponentially inversely dependent on the sputter rate, the use of smaller raster sizes (<75 microns) with smaller field apertures (<30 microns) while retaining high primary beam current ($\sim$20 nA) will lead to near constant background intensities, even in variably hydrated glasses. Detecting the NO^- species is also advisable for future studies, as the high sputtering rate of a Cs^+ primary beam results in near equal count rates to N^+, even though the useful yields are lower. In addition, the high sputter rate produces lower and more constant background than a O^- primary ion beam. In this case, analysts must again 1) use matrix-matched standards with appropriate water contents to determine correct calibration factors, and 2) maximize sputter rate. In either case, ion-implanted matrices can and should be used to unambiguously record matrix effects and serve as ideal matrix-matched standards.

REFERENCES

Ardia, P., Di Muro, A., Giordano, D., Massare, D., Sanchez-Valle, C., Schmidt, M., 2014. Densification mechanisms of haplogranite glasses as a function of water content and pressure based on density and Raman data. Geochimica et Cosmochimica Acta 138, 158–180.

Behrens, H., Tamic, N., Holtz, F., 2004. Determination of the molar absorption coefficient for the infrared absorption band of CO_2 in rhyolitic glasses. American Mineralogist 89 (2-3), 301–306.

Burnett, D. S., Jurewicz, A. J., Woolum, D. S., Wang, J., Paque, J. M., Nittler, L. R., McKeegan, K. D., Humayun, M., Hervig, R., Heber, V. S., Guan, Y., 2015. Ion implants as matrix-appropriate calibrators for geochemical ion probe analyses. Geostandards and Geoanalytical Research 39 (3), 265–276.

Canfield, D. E., Glazer, A. N., Falkowski, P. G., 2010. The evolution and future of earth's nitrogen cycle. Science 330 (6001), 192–196.

Cartigny, P., Marty, B., 2013. Nitrogen isotopes and mantle geodynamics: The emergence of life and the atmosphere–crust–mantle connection. Elements 9 (5), 359–366.

Chen, J., Schauer, S., Hervig, R., 2013. Normal-incidence electron gun alignment method for negative ion analysis on insulators by magnetic sector SIMS. Nuclear Instruments and Methods in Physics Research Section B: Beam Interactions with Materials and Atoms 295, 50–54.

Christiansen, R. L., 1984. Yellowstone magmatic evolution: Its bearing on understanding large-volume explosive volcanism, in: Explosive Volcanism. Its Inception, Evolution and Hazards. National Academy Press Washington, DC, pp. 84–95.

Christiansen, R. L., 2001. The Quaternary and Pliocene Yellowstone Plateau volcanic field of Wyoming, Idaho, and Montana. Tech. Rep. 729-G, U.S. Geological Survey Professional Paper.

Devine, J. D., Gardner, J. E., Brack, H. P., Laynet, G. D., Rutherford, M. J., 1995. Comparison of microanalytical methods for estimating H_2O contents of silicic volcanic glasses. American Mineralogist 80 (3-4), 319–328.

Dixon, J. E., Stolper, E. M., Holloway, J. R., 1995. An experimental study of water and carbon dioxide solubilities in mid-ocean ridge basaltic liquids. Part I: calibration and solubility models. Journal of Petrology 36 (6), 1607–1631.

Dunbar, N. W., Hervig, R. L., 1992. Petrogenesis and volatile stratigraphy of the Bishop Tuff: evidence from melt inclusion analysis. Journal of Geophysical Research: Solid Earth 97 (B11), 15,129–15,150.

Elkins, L. J., Fischer, T. P., Hilton, D. R., Sharp, Z. D., McKnight, S., Walker, J., 2006. Tracing nitrogen in volcanic and geothermal volatiles from the Nicaraguan volcanic front. Geochimica et Cosmochimica Acta 70 (20), 5215–5235.

Fischer, T. P., 2008. Fluxes of volatiles (H_2O, CO_2, N_2, Cl, F) from arc volcanoes. Geochemical Journal 42 (1), 21–38.

Fogel, R. A., Rutherford, M. J., 1990. The solubility of carbon dioxide in rhyolitic melts; a quantitative FTIR study. American Mineralogist 75 (11-12), 1311–1326.

Franzreb, K., Lörinčík, J., Williams, P., 2004. Quantitative study of oxygen enhancement of sputtered ion yields. I. Argon ion bombardment of a silicon surface with O_2 flood. Surface Science 573 (2), 291–309.

Galloway, J. N., 1998. The global nitrogen cycle: changes and consequences. Environmental Pollution 102 (1), 15–24.

Goldblatt, C., Claire, M. W., Lenton, T. M., Matthews, A. J., Watson, A. J., Zahnle, K. J., 2009. Nitrogen-enhanced greenhouse warming on early earth. Nature Geoscience 2 (12), 891–896.

Grob, J.-J., 2013. Ion implantation, in: Baudrant, A. (Ed.), Silicon Technologies: Ion Implantation and Thermal Treatment. John Wiley & Sons, Inc., Hoboken, NJ, Ch. 2.

Hauri, E., Wang, J., Dixon, J. E., King, P. L., Mandeville, C., Newman, S., 2002. SIMS analysis of volatiles in silicate glasses: 1. Calibration, matrix effects and comparisons with FTIR. Chemical Geology 183 (1), 99–114.

Hauri, E. H., Shaw, A. M., Wang, J., Dixon, J. E., King, P. L., Mandeville, C., 2006. Matrix effects in hydrogen isotope analysis of silicate glasses by SIMS. Chemical Geology 235 (3), 352–365.

Hervig, R. L., Mazdab, F. K., Williams, P., Guan, Y., Huss, G. R., Leshin, L. A., 2006. Useful ion yields for Cameca IMS 3f and 6f SIMS: Limits on quantitative analysis. Chemical Geology 227 (1), 83–99.

Hervig, R. L., Moore, G. M., Roggensack, K., 2009. Calibrating carbon measurements in basaltic glass using SIMS and FTIR: The effect of variable H_2O contents. In: AGU Fall Meeting Abstracts. Vol. 1. p. 1755.

Hildreth, W., Wilson, C. J. N., 2007. Compositional zoning of the Bishop Tuff. Journal of Petrology 48 (5), 951–999.

Hilton, D. R., Fischer, T. P., Marty, B., 2002. Noble gases and volatile recycling at subduction zones. Reviews in Mineralogy and Geochemistry 47 (1), 319–370.

Johnson, B., Goldblatt, C., 2015. The nitrogen budget of earth. Earth-Science Reviews 148, 150–173.

Kesson, S. E., Holloway, J. R., 1974. Generation of N_2-CO_2-H_2O fluids for use in hydrothermal experimentation. 2. Melting of albite in a multispecies fluid. American Mineralogist 59 (5-6), 598–603.

Leschik, M., Heide, G., Frischat, G., Behrens, H., Wiedenbeck, M., Wagner, N., Heide, K., Geißler, H., Reinholz, U., 2004. Determination of H_2O and D_2O contents in rhyolitic glasses. Physics and Chemistry of Glasses 45 (4), 238–251.

Li, Y., Huang, R., Wiedenbeck, M., Keppler, H., 2015. Nitrogen distribution between aqueous fluids and silicate melts. Earth and Planetary Science Letters 411, 218–228.

Li, Y., Wiedenbeck, M., Shcheka, S., Keppler, H., 2013. Nitrogen solubility in upper mantle minerals. Earth and Planetary Science Letters 377, 311–323.

Libourel, G., Marty, B., Humbert, F., 2003. Nitrogen solubility in basaltic melt. Part I. Effect of oxygen fugacity. Geochimica et Cosmochimica Acta 67 (21), 4123–4135.

Liu, Y., Anderson, A. T., Wilson, C. J., Davis, A. M., Steele, I. M., 2006. Mixing and differentiation in the Oruanui rhyolitic magma, Taupo, New Zealand: evidence from volatiles and trace elements in melt inclusions. Contributions to Mineralogy and Petrology 151 (1), 71–87.

Lowe, D. J., Blaauw, M., Hogg, A. G., Newnham, R. M., 2013. Ages of 24 widespread tephras erupted since 30,000 years ago in New Zealand, with re-evaluation of the timing and palaeoclimatic implications of the Lateglacial cool episode recorded at Kaipo Bog. Quaternary Science Reviews 74, 170–194.

Lowe, D. J., Shane, P. A., Alloway, B. V., Newnham, R. M., 2008. Fingerprints and age models for widespread New Zealand tephra marker beds erupted since 30,000 years ago: a framework for NZ-INTIMATE. Quaternary Science Reviews 27 (1), 95–126.

Luhr, J. F., 2001. Glass inclusions and melt volatile contents at Paricutin Volcano, Mexico. Contributions to Mineralogy and Petrology 142 (3), 261–283.

Marty, B., 1995. Nitrogen content of the mantle inferred from N_2–Ar correlation in oceanic basalts. Nature 377 (6547), 326–329.

Marty, B., Zimmermann, L., Pujol, M., Burgess, R., Philippot, P., 2013. Nitrogen isotopic composition and density of the Archean atmosphere. Science 342 (6154), 101–104.

Mason, B. G., Pyle, D. M., Oppenheimer, C., 2004. The size and frequency of the largest explosive eruptions on earth. Bulletin of Volcanology 66 (8), 735–748.

Mikhail, S., Sverjensky, D. A., 2014. Nitrogen speciation in upper mantle fluids and the origin of Earth's nitrogen-rich atmosphere. Nature Geoscience 7 (11), 816–819.

Miyazaki, A., Hiyagon, H., Sugiura, N., Hirose, K., Takahashi, E., 2004. Solubilities of nitrogen and noble gases in silicate melts under various oxygen fugacities: implications for the origin and degassing history of nitrogen and noble gases in the Earth. Geochimica et Cosmochimica Acta 68 (2), 387–401.

Moore, G., Roggensack, K., Klonowski, S., 2008. A low-pressure–high-temperature technique for the piston-cylinder. American Mineralogist 93 (1), 48–52.

Mulfinger, H., 1966. Physical and chemical solubility of nitrogen in glass melts. Journal of the American Ceramic Society 49 (9), 462–467.

Mulfinger, V., Dietzel, A., Navarro, J., 1972. Physical solubility of helium, neon, and nitrogen in glass melts. Glastechnische Berichte Glass Science and Technology 45 (9), 389–96.

Myers, M., Wallace, P., Wilson, C., Morter, B., Swallow, E., in press. Prolonged ascent and episodic venting of discrete magma batches at the onset of the Huckleberry Ridge supereruption, Yellowstone. Earth and Planetary Science Letters.

Mysen, B. O., Virgo, D., Harrison, W. J., Scarfe, C. M., 1980. Solubility mechanisms of H_2O in silicate melts at high pressures and temperatures: a Raman spectroscopic study. American Mineralogist 65, 900–914.

Newman, S., Stolper, E. M., Epstein, S., 1986. Measurement of water in rhyolitic glasses: Calibration of an infrared spectroscopic technique. American Mineralogist 71 (11-12), 1527–1541.

Nuccio, P., Paonita, A., 2000. Investigation of the noble gas solubility in H_2O–CO_2 bearing silicate liquids at moderate pressure ii: the extended ionic porosity (EIP) model. Earth and Planetary Science Letters 183 (3), 499–512.

Nuccio, P. M., Paonita, A., 2001. Magmatic degassing of multicomponent vapors and assessment of magma depth: application to Vulcano Island (Italy). Earth and Planetary Science Letters 193 (3), 467–481.

Raymond, J., Siefert, J. L., Staples, C. R., Blankenship, R. E., 2004. The natural history of nitrogen fixation. Molecular biology and evolution 21 (3), 541–554.

Richet, P., Whittington, A., Holtz, F., Behrens, H., Ohlhorst, S., Wilke, M., 2000. Water and the density of silicate glasses. Contributions to Mineralogy and Petrology 138 (4), 337–347.

Roggensack, K., Hervig, R. L., McKnight, S. B., Williams, S. N., 1997. Explosive basaltic volcanism from Cerro Negro volcano: influence of volatiles on eruptive style. Science 277 (5332), 1639–1642.

Sano, Y., Takahata, N., Nishio, Y., Fischer, T. P., Williams, S. N., 2001. Volcanic flux of nitrogen from the earth. Chemical Geology 171 (3), 263–271.

Schauer, S. N., Williams, P., 1990. Elimination of cluster interferences in secondary ion mass spectrometry using extreme energy filtering. International Journal of Mass Spectrometry and Ion Processes 103 (1), 21–29.

Singer, B. S., Jicha, B. R., Condon, D. J., Macho, A. S., Hoffman, K. A., Dierkhising, J., Brown, M. C., Feinberg, J. M., Kidane, T., 2014. Precise ages of the Réunion event and Huckleberry Ridge excursion: Episodic clustering of geomagnetic instabilities and the dynamics of flow within the outer core. Earth and Planetary Science Letters 405, 25–38.

Skirius, C. M., 1990. Pre-eruptive H_2O and CO_2 content of plinian and ash-flow Bishop Tuff magma. Ph.D. thesis, University of Chicago, Department of the Geophysical Sciences.

Stephant, A., Remusat, L., Thomen, A., Robert, F., 2014. Reduction of OH contamination in quantification of water contents using NanoSIMS imaging. Chemical Geology 380, 20–26.

Tenner, T. J., Hirschmann, M. M., Withers, A. C., Hervig, R. L., 2009. Hydrogen partitioning between nominally anhydrous upper mantle minerals and melt between 3 and 5 GPa and applications to hydrous peridotite partial melting. Chemical Geology 262 (1), 42–56.

Tsipenyuk, Y. M., Chapyzhnikov, B. A., Kolotov, V. P., Shilobreeva, S. N., Kadik, A. A., 1997. Gamma-activation analysis of nitrogen solubility in alumosilicates at high pressure and temperature. Journal of Radioanalytical and Nuclear Chemistry 217 (2), 261–265.

Vandergoes, M. J., Hogg, A. G., Lowe, D. J., Newnham, R. M., Denton, G. H., Southon, J., Barrell, D. J., Wilson, C. J., McGlone, M. S., Allan, A. S., et al., 2013. A revised age for the Kawakawa/Oruanui tephra, a key marker for the Last Glacial Maximum in New Zealand. Quaternary Science Reviews 74, 195–201.

Wallace, P. J., 2005. Volatiles in subduction zone magmas: concentrations and fluxes based on melt inclusion and volcanic gas data. Journal of Volcanology and Geothermal Research 140 (1), 217–240.

Wallace, P. J., Anderson, A. T., Davis, A. M., 1999. Gradients in H_2O, CO_2, and exsolved gas in a large-volume silicic magma system: Interpreting the record preserved in melt inclusions from the Bishop Tuff. Journal of Geophysical Research: Solid Earth 104 (B9), 20097–20122.

Wilson, C. J. N., Charlier, B. L. A., 2009. Rapid rates of magma generation at contemporaneous magma systems, Taupo Volcano, New Zealand: Insights from U–Th model-age spectra in zircons. Journal of Petrology 50 (5), 875–907.

Wilson, C. J. N., Houghton, B. F., McWilliams, M. O., Lanphere, M. A., Weaver, S. D., Briggs, R. M., 1995. Volcanic and structural evolution of Taupo Volcanic Zone, New Zealand: a review. Journal of Volcanology and Geothermal Research 68 (1), 1–28.

Wilson, C. J. N., Rogan, A. M., Smith, I. E. M., Northey, D. J., Nairn, I. A., Houghton, B. F., 1984. Caldera volcanoes of the Taupo volcanic zone, New Zealand. Journal of Geophysical Research: Solid Earth 89 (B10), 8463–8484.

Wilson, R. G., Stevie, F. A., Magee, C. W., 1989. Secondary ion mass spectrometry: a practical handbook for depth profiling and bulk impurity analysis. Wiley-Interscience, New York.

Withers, A. C., Behrens, H., 1999. Temperature-induced changes in the NIR spectra of hydrous albitic and rhyolitic glasses between 300 and 100 K. Physics and Chemistry of Minerals 27 (2), 119–132.

Wordsworth, R., Pierrehumbert, R., 2013. Hydrogen-nitrogen greenhouse warming in earth's early atmosphere. Science 339 (6115), 64–67.

Zhang, Y., Belcher, R., Ihinger, P. D., Wang, L., Xu, Z., Newman, S., 1997. New calibration of infrared measurement of dissolved water in rhyolitic glasses. Geochimica et Cosmochimica Acta 61 (15), 3089–3100.

Zhang, Y. H., Navrotsky, A., Matusch, D., Seifert, H. J., 2003. Energetics of oxidation of RE-Si-Al-ON glasses. Journal of Materials Research 18 (7), 1607–1613.

APPENDIX A

MELT INCLUSION VOLATILE CONTENTS

Locality	Unit	H_2O (wt.%)	CO_2 (ppm)	N (ppm)
Bishop Tuff				
f1-1a	Early erupted	4.32(0.01)	0.0(0.0)	0.0(0.0)
f1-1a	Early erupted	5.07(0.02)	40.8(61.4)	6.46(3.2)
f1-1a	Early erupted	4.98(0.01)	22.0(63.5)	4.68(3.3)
f1-1a	Early erupted	4.06(0.01)	91.5(66.2)	16.0(4.4)
f1-1a	Early erupted	5.45(0.02)	66.2(65.2)	15.3(4.0)
f1-1a	Early erupted	4.78(0.06)	147.1(64.2)	11.4(3.8)
f1-1a	Early erupted	4.66(0.02)	63.6(65.4)	21.9(4.9)
f1-1a	Early erupted	5.09(0.02)	168.6(64.0)	21.0(3.8)
f1-1a	Early erupted	4.23(0.02)	206.6(56.8)	20.8(3.8)
f1-6a	Early erupted	5.85(0.02)	124.9(31.3)	0.40(0.7)
f1-6a	Early erupted	5.83(0.01)	107.9(31.9)	1.08(0.8)
f1-6a	Early erupted	5.33(0.01)	158.0(32.9)	1.70(0.9)
f1-6a	Early erupted	5.25(0.01)	172.7(32.9)	6.45(1.2)
f1-6a	Early erupted	5.39(0.01)	173.4(33.4)	13.9(1.8)
f1-6a	Early erupted	3.97(0.01)	60.9(36.5)	1.35(1.2)
f1a-FTIR	Early erupted	3.53(0.76)	75.6(15.4)	44.2(4.1)
f1a-FTIR	Early erupted	3.52(0.56)	18.9(2.9)	21.4(5.3)
f1a-FTIR	Early erupted	3.48(0.75)	32.1(6.4)	14.6(2.9)
f1a-FTIR	Early erupted	4.93(1.39)	43.4(11.4)	28.2(3.4)
f1a-FTIR	Early erupted	4.13(0.99)	8.0(1.8)	10.0(10.8)
f1b-FTIR	Early erupted	5.37(0.53)	0.0(0.0)	20.5(4.1)
f1b-FTIR	Early erupted	5.70(0.13)	54.9(5.1)	32.0(6.4)
f1b-FTIR	Early erupted	5.30(0.12)	39.2(4.1)	21.3(4.3)
f1b-FTIR	Early erupted	5.31(0.02)	26.7(0.4)	17.0(3.4)
BB-105	Middle erupted	3.38(0.01)	17.6(107.9)	3.04(1.6)
BB-105	Middle erupted	3.10(0.01)	228.5(110.7)	5.52(1.5)
BB-105	Middle erupted	3.05(0.01)	2.33(105.0)	5.53(1.5)
BB-105	Middle erupted	3.75(0.01)	274.5(106.9)	11.5(2.2)
BB-105	Middle erupted	3.06(0.01)	0.0(0.0)	2.90(1.5)
BB-105	Middle erupted	2.86(0.01)	0.0(0.0)	4.35(1.5)
BB-105	Middle erupted	3.61(0.01)	186.3(109.1)	8.94(1.9)
327-3-1	Late erupted	3.47(0.01)	641.6(35.2)	3.66(1.2)
327-3-1	Late erupted	3.44(0.01)	690.3(40.4)	6.47(1.3)
327-3-1	Late erupted	2.08(0.01)	692.0(50.4)	8.98(2.3)
327-3-1	Late erupted	2.68(0.01)	350.8(32.3)	2.71(1.2)
327-3-1	Late erupted	3.78(0.01)	803.4(38.9)	5.34(1.2)
327-3-1	Late erupted	3.63(0.01)	630.1(39.4)	4.93(1.5)
Huckleberry Ridge Tuff				
mm4	Early erupted	2.43(0.01)	0.00(0.0)	5.49(1.4)

mm4	Early erupted	2.21(0.01)	150.6(20.4)	6.34(1.5)
mm4	Early erupted	2.58(0.02)	327.8(19.3)	8.76(1.5)
mm4	Early erupted	2.44(0.01)	338.6(18.5)	7.06(1.3)
mm4	Early erupted	1.21(0.01)	723.6(33.6)	23.3(3.2)
mm4	Early erupted	1.20(0.01)	481.8(23.3)	6.26(2.3)
mm4	Early erupted	2.65(0.01)	77.6(16.1)	3.91(1.1)
mm5	Early erupted	2.69(0.01)	426.2(18.3)	4.08(0.4)
mm5	Early erupted	2.44(0.02)	424.4(18.0)	5.48(0.5)
mm5	Early erupted	1.69(0.01)	0.0(0.0)	12.2(0.7)
mm5	Early erupted	2.44(0.01)	582.4(69.3)	13.2(1.1)
mm5	Early erupted	2.74(0.01)	85.0(12.0)	6.90(0.7)
mm5	Early erupted	3.28(0.01)	762.1(30.1)	7.72(1.4)
mm5	Early erupted	3.02(0.01)	646.1(24.7)	7.05(1.2)
mm5	Early erupted	2.76(0.02)	665.9(25.6)	9.69(1.0)
Taupo Volcanic Center				
Okaia	N/A	2.00(0.01)	107.5(25.7)	8.21(4.6)
Okaia	N/A	3.17(0.01)	779.0(93.0)	20.2(4.0)
Okaia	N/A	3.69(0.01)	294.9(55.8)	13.0(3.2)
Okaia	N/A	3.96(0.02)	827.5(61.9)	28.9(4.4)
Okaia	N/A	2.94(0.01)	0.0(0.0)	8.75(3.0)
Oruanui	Basal Unit	4.91(0.01)	182.1(41.4)	12.1(1.8)
Oruanui	Basal Unit	3.64(0.01)	210.7(28.5)	15.9(2.3)
Oruanui	Basal Unit	1.59(0.01)	544.1(32.7)	36.0(5.3)
Oruanui	Basal Unit	5.78(0.01)	314.2(38.3)	26.7(2.8)

Errors, in parentheses, are given in 1 sigma. Concentrations of 0 are those that were negative after background subtraction. All concentrations were determined by SIMS except the H_2O and CO_2 measurements of f1a-FTIR and f1b-FTIR melt inclusions.